

# Airglow data-driven modeling over a period of three solar cycles

Simon Mackovjak<sup>1</sup>, Matej Varga<sup>2</sup>, Stanislav Hrivňak<sup>3</sup>, Ondrej Palkoci<sup>3</sup>, and Goderdzi Didebulidze<sup>4</sup>

<sup>1</sup>Institute of Experimental Physics

<sup>2</sup>Faculty of Electrical Engineering and Informatics, Technical University of Kosice

<sup>3</sup>GlobalLogic s.r.o.

<sup>4</sup>Iliia State University

November 30, 2022

## Abstract

The Earth's upper atmosphere is a dynamic environment that is continuously affected by space weather from above and atmospheric processes from below. An effective way to observe this interface region is the monitoring of airglow. Since the 1950s, airglow emissions have been systematically measured by ground-based photometers in specific wavelength bands during the nighttime. The availability of the calibrated data from over 30 years of photometric airglow measurements at Abastumani in Georgia (41.75 N, 42.82 E), at wavelengths of 557.7 nm and 630.0 nm, enable us to investigate if a data-driven model based on advanced machine learning techniques can be successfully employed for modeling airglow intensities. A regression task was performed using the time series of space weather indices and thermosphere-ionosphere parameters. We have found that the developed data-driven model has good consistency with the commonly used GLOW airglow model and also captures airglow variations caused by cycles of solar activity and changes of the seasons. This enables us to visualize the green and red airglow variations over a period of three solar cycles with a one-hour time resolution.

# Data-driven modeling of atomic oxygen airglow over a period of three solar cycles

Š. Mackovjak<sup>1,3</sup>, M. Varga<sup>2</sup>, S. Hrivňak<sup>3</sup>, O. Palkoci<sup>3</sup>, G. G. Didebulidze<sup>4</sup>

<sup>1</sup>Department of Space Physics, Institute of Experimental Physics, Slovak Academy of Sciences, Košice, Slovakia

<sup>2</sup>Department of Cybernetics and Artificial Intelligence, Faculty of Electrical Engineering and Informatics, Technical University of Košice, Košice, Slovakia

<sup>3</sup>GlobalLogic Slovakia s.r.o., Košice, Slovakia

<sup>4</sup>Georgian National Astrophysical Observatory, Ilia State University, Tbilisi, Georgia

## Key Points:

- A data-driven model is able to represent complex physical phenomena
- Advanced machine learning techniques are effective for the development of the data-driven model
- Developed data-driven model visualizes airglow hourly intensities over a 30-year period for location Abastumani (41.75° N, 42.82° E)

---

Corresponding author: Šimon Mackovjak, Institute of Experimental Physics SAS, Watsonova 47, 04001 Košice, Slovakia, [mackovjak@saske.sk](mailto:mackovjak@saske.sk)

## 16 **Abstract**

17 The Earth's upper atmosphere is a dynamic environment that is continuously affected  
18 by space weather from above and atmospheric processes from below. An effective way  
19 to observe this interface region is the monitoring of airglow. Since the 1950s, airglow emis-  
20 sions have been systematically measured by ground-based photometers in specific wave-  
21 length bands during the nighttime. The availability of the calibrated data from over 30  
22 years of photometric airglow measurements at Abastumani in Georgia (41.75° N, 42.82°  
23 E), at wavelengths of 557.7 nm and 630.0 nm, enable us to investigate if a data-driven  
24 model based on advanced machine learning techniques can be successfully employed for  
25 modeling airglow intensities. A regression task was performed using the time series of  
26 space weather indices and thermosphere-ionosphere parameters. We have found that the  
27 developed data-driven model has good consistency with the commonly used GLOW air-  
28 glow model and also captures airglow variations caused by cycles of solar activity and  
29 changes of the seasons. This enables us to visualize the green and red airglow variations  
30 over a period of three solar cycles with a one-hour time resolution.

## 31 **1 Introduction**

32 The Earth's upper atmosphere acts as an interface between processes in space and  
33 on Earth. It is a very dynamic environment continuously influenced by solar radiation  
34 and space weather from above and by atmospheric weather and electrical discharges from  
35 below (Pfaff, 2012). An effective way to monitor these dynamics during night-time pe-  
36 riods in the altitude range of 80–300 km is observation of airglow (Khomich et al., 2008).  
37 Airglow is a non-thermal emission of light originating from excited atomic or molecu-  
38 lar states. The source of the excitation, directly or indirectly, is the solar electromag-  
39 netic radiation (von Savigny, 2017). The particular process responsible for the emission  
40 of airglow and the amount of this emission is mainly dependent on the composition and  
41 concentrations of neutral constituents and ion/electron densities in the thermosphere-  
42 ionosphere system.

43 The earliest reported airglow variation is connected to the 11-year long solar cy-  
44 cle. The correlation between the well-known atomic oxygen  $\text{OI}(^1\text{D}_2 - ^1\text{S}_0)$  airglow emis-  
45 sion of the green line (557.7 nm) with sunspot area was revealed in 1935 (Rayleigh & Jones,  
46 1935). The connection of solar activity, expressed by solar flux index F10.7 was confirmed  
47 by extensive studies (Deutsch & Hernandez, 2003; Liu & Shepherd, 2008; Reid et al., 2014).

48 The authors provide clear evidence that the green line intensity is maximal during the  
49 maximum of the solar cycle. The variations within the year (annual oscillation and semi-  
50 annual oscillation) are associated with the yearly tilt and rotation of the Earth around  
51 the Sun and also with the dynamics in the whole atmosphere, mainly driven by atmo-  
52 spheric tides. The amplitude and maximum of a period are different for different loca-  
53 tions. Shepherd et al. (2006) and Liu et al. (2008) used UARS/WINDII (Shepherd et  
54 al., 1993) space-based observations of the green line in the years 1991–1997 to present  
55 airglow variations during the year for different latitudes. The authors concluded that for  
56 the equatorial region, semi-annual variation has maxima at equinoxes and for the mid-  
57 latitude regions, the annual variation is dominant and has a maximum in autumn in the  
58 northern hemisphere and in spring in the southern hemisphere. There are also shorter  
59 and non-periodic variations in the upper atmosphere. The influence of geomagnetic storms  
60 has been observed in airglow intensity measurements since the mid-twentieth century  
61 (Silverman, 1970). During a geomagnetic storm, the density distribution of the ions and  
62 neutral constituents in the upper atmosphere varies dramatically. Such variations may  
63 have signatures in airglow emissions (Leonovich et al., 2011; Makela et al., 2014; Bag et  
64 al., 2017).

65 Although some patterns in airglow variations were recognized, a clear physical ex-  
66 planation is still missing. This is a consequence of the very high complexity of the en-  
67 vironment and the fact that the response of airglow production might be not uniformly  
68 related to a single process. Indeed, airglow intensity represents the continuous variation  
69 of solar activity, solar wind, interplanetary magnetic field, magnetospheric drivers as well  
70 as non-constant density and temperature conditions in the upper atmosphere together  
71 with ever-present vertical motions from lower atmosphere including tides, planetary waves,  
72 and atmospheric gravity waves. The ionosphere-thermosphere system is also affected by  
73 alteration of the global ionosphere electric potential and by various ionospheric insta-  
74 bilities such as plasma bubbles and ionospheric scintillation (Eastes et al., 2019). As the  
75 understanding of consequences of these processes is still not sufficient, the whole sub-  
76 ject is very topical and it is an objective of several ground-based and space-based mis-  
77 sions (e.g. Eastes et al., 2017; Immel et al., 2018; Hannawald et al., 2019; Mackovjak et  
78 al., 2019; Wüst et al., 2019).

79 Data-driven machine learning techniques have become effective tools in space sci-  
80 ence in recent years (e.g. Ball & Brunner, 2010; George & Huerta, 2018; Zucker & Giryes,

2018). It is mainly due to the fact that the huge amount of space data can be effectively processed by powerful computing units utilizing open source frameworks supported by technology giants (e.g. Pedregosa et al., 2011; Abadi et al., 2015; Paszke et al., 2017). A comprehensive overview of the machine learning techniques and their application for space weather research is presented by Camporeale et al. (2018). The aim of this paper is to investigate if a data-driven approach using machine learning techniques can provide adequate results of long-term airglow intensity modeling. The usefulness of this approach will be evaluated by its capability to reproduce generally known airglow variations as well as by comparison with the output from the Global Airglow (GLOW) model (Solomon et al., 1988; Solomon, 2017; Hirsch & Solomon, 2019). The data and machine learning methods used are described in Section 2. The results obtained and discussion are presented together in Section 3. Section 4 summarizes our work and describes the next steps in our research.

## 2 Data and Methods

Depending on the solar elevation, airglow can be categorized as dayglow, twilightglow and nightglow (von Savigny, 2017). Dayglow emission is the brightest but its observation is not straightforward due to the presence of direct and scattered light from the Sun. Therefore, every time the term airglow is used in this work, the nightglow (solar zenith angle ( $S_{ZA}$ ) is higher than  $108^\circ$ ) is considered. Our focus is on atomic oxygen emissions - green line and red line with the wavelengths 557.7 nm and 630.0 nm, respectively. The details of their emission production mechanisms are presented in Khomich et al. (2008).

The main dataset used consists of calibrated photometric data of the airglow green line (557.7 nm) and airglow red line (630.0 nm) measured at Abastumani in Georgia ( $41.75^\circ$  N,  $42.82^\circ$  E, 1,580 m above sea level) in the years 1957–1993 (Fishkova, 1983; Gudadze et al., 2007; Didebulidze et al., 2011; NDMC, (last access: November 30, 2020)). Measured intensities are in units of Rayleighs ( $1 \text{ R} = 10^{10} \text{ photon m}^{-2} \text{ s}^{-1}$ ). They were acquired during the moonless (moon zenith angle ( $M_{ZA}$ ) is higher than  $90^\circ$ ) and cloudless conditions. The time resolution of the data is 6–15 minutes. For the purposes of this work, hourly averages were used within the time interval 1964–1993. The boxplots of the measured data are displayed in Figure 1. They represent the distributions of the measurements over the years. The total amount of data used is  $\sim 3,850$  measurements, rep-

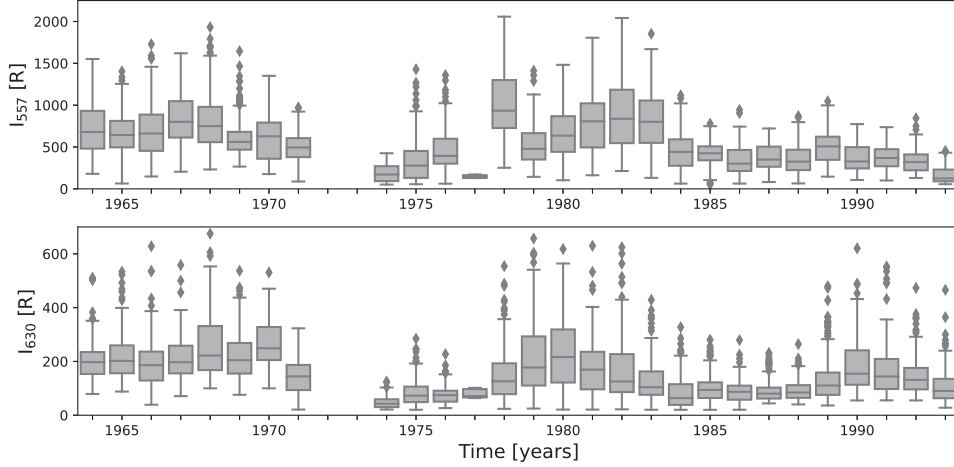


**Figure 1.** The box plots of the airglow measurements at Abastumani (Georgia) over the years 1964–1993. Only the hourly averages are considered where the sunless, moonless, and cloudless conditions are satisfied. Each interquartile range is represented by the particular box and the median of the distribution is marked with a horizontal dash. The diamond points outside the box whiskers represent the outliers caused by high variability of the measurements. They are not caused by an experimental error and they can be used in the analysis.

Distributions of the green line and red line intensities are displayed on the top and bottom, respectively.

113 resenting  $\sim 8\%$  of all possible dark night hours (hours when  $S_{ZA} > 108^\circ$  &  $M_{ZA} > 90^\circ$ )  
 114 over a 30-year period for this location. One of the goals of this work is to model the air-  
 115 glow green and red line intensities for the rest of the dark night hours (i.e.  $\sim 92\%$ ) in  
 116 this period.

117 In the data-driven modeling approach, the measured airglow intensities were used  
 118 as labels (target outputs). The features (inputs) for the model were chosen from four cat-  
 119 egories: space weather indices, thermosphere parameters, ionosphere parameters, and  
 120 Sun-Earth distance. These four categories cover the basic processes that affect airglow  
 121 intensities. Although the exact physical relations between these features (inputs) and  
 122 labels (target outputs) are not considered here, it is assumed that these underlying re-  
 123 lations are present in the data. Machine learning techniques should be able to recognize  
 124 these underlying relations and also model airglow intensities for previously unseen fea-  
 125 ture values. For the appropriate feature selection, all available data from the OMNIWeb

**Table 1.** The selected features for machine learning techniques to model airglow intensities

Feature	Units	Description	Source
F10.7 index	SFU	Solar radio flux per frequency ( $\lambda = 10.7$ cm)	OMNIWeb <sup>a</sup>
Kp index		Geomagnetic planetary K-index	OMNIWeb <sup>a</sup>
Dst index	nT	Geomagnetic equatorial index	OMNIWeb <sup>a</sup>
Neutral Temperature	K	Temperature of neutral atmosphere	NRLMSISE-00 <sup>b</sup>
Total Mass Density	g/cm <sup>3</sup>	Total mass density of neutral atmosphere	NRLMSISE-00 <sup>b</sup>
O	N/cm <sup>3</sup>	Atomic oxygen density	NRLMSISE-00 <sup>b</sup>
O <sub>2</sub>	N/cm <sup>3</sup>	Molecular oxygen density	NRLMSISE-00 <sup>b</sup>
N	N/cm <sup>3</sup>	Atomic nitrogen density	NRLMSISE-00 <sup>b</sup>
N <sub>2</sub>	N/cm <sup>3</sup>	Molecular nitrogen density	NRLMSISE-00 <sup>b</sup>
H	N/cm <sup>3</sup>	Atomic hydrogen density	NRLMSISE-00 <sup>b</sup>
T <sub>e</sub>	K	Temperature of electrons	IRI-2016 <sup>c</sup>
n <sub>e</sub>	N/m <sup>3</sup>	Density of electrons	IRI-2016 <sup>c</sup>
h <sub>m</sub> F <sub>2</sub>	km	F <sub>2</sub> layer peak height	IRI-2016 <sup>c</sup>
N <sub>m</sub> F <sub>2</sub>	N/m <sup>3</sup>	F <sub>2</sub> layer peak density	IRI-2016 <sup>c</sup>
Sun-Earth	AU	Sun-Earth distance	PyEphem <sup>d</sup>

<sup>a</sup>Available at: <https://omniweb.gsfc.nasa.gov/form/dx1.html> (King & Papitashvili, 2005)

<sup>b</sup>Available at: <https://ccmc.gsfc.nasa.gov/modelweb/models/nrlmsise00.php> (Picone et al., 2002)

<sup>c</sup>Available at: [https://ccmc.gsfc.nasa.gov/modelweb/models/iri2016\\_vitmo.php](https://ccmc.gsfc.nasa.gov/modelweb/models/iri2016_vitmo.php) (Bilitza et al., 2017)

<sup>d</sup>Available at: <https://pypi.org/project/pyephem>

126 space weather database (King & Papitashvili, 2005), NRLMSISE-00 thermosphere model  
 127 (Picone et al., 2002), and IRI-2016 ionosphere model (Bilitza et al., 2017) were explored.  
 128 These data are accessible in hourly resolution. The availability of the features for a 30-  
 129 year interval was considered in the feature selection process. The parameters of the neu-  
 130 tral atmospheres and ionosphere are obtained for the nominal altitudes 95 km and 250 km  
 131 for modeling green and red line, respectively. These are the altitudes of particular peak  
 132 airglow layer emissions (von Savigny, 2017). The feature selection was mainly guided by  
 133 current physical understanding of the features' influence on airglow production and also  
 134 on automatic data characterization methods. Automatic methods such as univariate fea-  
 135 ture selection and recursive selection of the features based on the model training pro-  
 136 cess (Pedregosa et al., 2011) have been examined for the exclusion of the redundant fea-  
 137 tures by quantification of their mutual correlation and by other statistical tests. The list  
 138 of 15 features selected for our work is presented in Table 1. We would like to mention  
 139 that none of the investigated features had a significant correlation with airglow inten-  
 140 sities. The absolute value of pairwise Pearson correlation coefficient was not higher than  
 141 0.26 for any pair of feature and label. It is noted that consideration of additional fea-  
 142 tures did not lead to better results. This does not mean the irrelevance of other indices  
 143 such as e.g. the interplanetary magnetic field or solar wind parameters. These indices  
 144 were excluded as their availability is less than 60% of the studied time interval.

145 The modeling of airglow intensities using the space weather indices, thermosphere-  
 146 ionosphere parameters, and Sun-Earth distances as the input is indeed a regression prob-  
 147 lem. Using known input and output values we would like to approximate the mapping  
 148 function that could provide, with sufficient precision, the airglow intensities as the out-  
 149 put for the previously unseen inputs. In the current work, we have employed the follow-  
 150 ing supervised machine learning techniques for the regression problem: linear regression,  
 151 Neural Networks, and the ensemble algorithms - Random Forest and Extreme Gradient  
 152 Boosting (XGBoost). Ordinary least squares linear regression, as the common statisti-  
 153 cal approach in astronomy (Isobe et al., 1990), was used as the simplest technique. The  
 154 Neural Network is one of the most popular machine learning techniques, although its us-  
 155 age is not always the best option, especially for problems where the features come from  
 156 different distributions (Fernández-Delgado et al., 2014). It is based on the fact that ev-  
 157 ery continuous real function over a compact set of real numbers can be approximated  
 158 arbitrarily well by a function defined as a Neural Network with a high enough number



159 of neurons. For more details refer to Cybenko (1989). In this work, we used a single hid-  
 160 den layer feed-forward Neural Network with a number of neurons 128-128-1 (i.e. 128 neu-  
 161 rons in the input layer, 128 neurons in the hidden layer, 1 neurons in the output layer),  
 162 hyperbolic tangent activation function, 300 learning epochs, and learning rate from 0.1  
 163 to 0.05 during the training. The choice of these hyper-parameters was based on pure ex-  
 164 perimentation with different values and optimizing for the metrics described below. The  
 165 Random Forest technique (Tin Kam Ho, 1998; Breiman, 2001) is a combination of de-  
 166 cision tree predictors. Indeed, it is an approach to average numerous decision trees to  
 167 obtain minimal variance. In this work, we used the Random Forest regressor with 100  
 168 decision trees and 15 maximum tree depth. The Random Forest technique is not as sen-  
 169 sitive to the specified hyper-parameters as Neural Network approach. Another very ef-  
 170 fective technique based on decision trees is Extreme Gradient Boosting - XGBoost (Chen  
 171 & Guestrin, 2016). It is an ensemble method that is developed to prevent overfitting,  
 172 handle missing values, allow parallel processing, and perform cross-validation at each it-  
 173 eration. It tries to find an optimal output using the gradient descent algorithm to min-  
 174 imize the loss for the newly created model. In this work, we used XGBoost regression  
 175 with squared loss, 0.05 learning rate, and 15 maximum tree depth. All the methods men-  
 176 tioned above are implemented and available in the libraries of the Python programming  
 177 language (Van Rossum & Drake, 2009) i.e. scikit-learn (Pedregosa et al., 2011) and Keras  
 178 (Chollet, 2015). Here, we have provided only a brief description. The specific set-up of  
 179 the machine learning techniques used and their hyper-parameters can be found in the  
 180 Jupyter notebook that is available as online material to this article (SPACE::LAB, 2020).

181 In order to characterize the performance of the techniques used, the following met-  
 182 rics were considered. The mean absolute error (MAE) represents the difference between  
 183 the true label value  $y_i$  of the airglow intensity and the corresponding modeled value  $\hat{y}_i$   
 184 of the  $i$ -th sample. It is defined as:

$$185 \quad MAE(y, \hat{y}) = \frac{1}{n} \sum_{i=1}^n |y_i - \hat{y}_i|, \quad (1)$$

186 for  $n$  number of samples. Due to the reason that the absolute intensities of green and  
 187 red airglow lines are different, we introduced also a relative metric the mean absolute  
 188 percentage error (MAPE). It allows us to compare the performance of the techniques used  
 189 for both airglow lines. Since the measured airglow intensity  $y_i$  will be always higher than

190 zero, the MAPE is defined as:

$$191 \quad MAPE(y, \hat{y}) = \frac{100\%}{n} \sum_{i=1}^n \frac{|y_i - \hat{y}_i|}{y_i}. \quad (2)$$

192 Due to the complexity of the upper atmosphere environment, the commonly used  
 193 models applied for calculation of airglow intensities are limited and do not contain all  
 194 the relevant processes. One of the most used, the Global Airglow (GLOW) model (Solomon  
 195 et al., 1988; Solomon, 2017; Hirsch & Solomon, 2019) provides emission rates for most  
 196 prominent airglow lines for particular altitude, latitude, longitude, and time. It uses en-  
 197 ergetic inputs from the Sun and aurora and also thermospheric parameters. It can also  
 198 employ the output from general atmosphere circulation models such as the Thermosphere-  
 199 Ionosphere-Electrodynamics General Circulation Model (TIE-GCM) (Roble et al., 1988;  
 200 Qian et al., 2014). The simulated airglow brightness over the whole Earth’s disk is qual-  
 201 itatively consistent with measurements from the most recent airglow space mission GOLD  
 202 (Global-scale Observations of the Limb and Disk) (Gan et al., 2020).

### 203 3 Results and Discussion

204 The objective of the present work is to model the intensities of the airglow green  
 205 line (557.7 nm) and red line (630.0 nm) for the period 1964–1993. For this purpose, we  
 206 employed the data and techniques described in Section 2. It is noted that the main dataset  
 207 was split into a subset for training and a subset for testing of each particular technique.  
 208 The subsets for training and testing contain 80 % and 20 % of all data from the main dataset,  
 209 respectively. The data for train and test subsets were selected randomly. The data from  
 210 the main dataset are shuffled and split equally for all techniques to assure reproducible  
 211 and comparable results. The comparison of the performance of the machine learning tech-  
 212 niques used against the same subset for testing is presented in Table 2.

213 For the purposes of quantifying the methods’ performance, the results from base-  
 214 line model are also listed. They were obtained by considering simple average of the val-  
 215 ues of training labels as the modeled value  $\hat{y}_i$ . As expected, the lowest performance was  
 216 obtained for the simplest method - linear regression. The Neural Network model pro-  
 217 vides significantly better results for MAE but even worse results for MAPE than the base-  
 218 line. This is a consequence of the fact that for some low values of  $y_i$ , the modeled value  
 219 of  $\hat{y}_i$  might be higher by hundreds of percent although in absolute values this difference  
 220 ( $|y_i - \hat{y}_i|$ ) is not so significant. Therefore it is instructive to examine the both the MAE

**Table 2.** The performance of machine learning techniques used for modeling of green (557.7 nm) and red (630.0 nm) airglow lines intensities.

	<b>I 557</b>		<b>I 630</b>	
	<b>MAE</b>	<b>MAPE</b>	<b>MAE</b>	<b>MAPE</b>
Baseline	265 R	78 %	84 R	86 %
Lin. Regression	247 R	65 %	77 R	72 %
Neural Network	146 R	95 %	63 R	90 %
Random Forest	102 R	23 %	53 R	41 %
XGBoost	88 R	16 %	48 R	32 %

221 and MAPE metrics presented in Table 2. The evidence that the neural networks might  
 222 be outperformed by techniques based on decision trees for limited datasets is well known  
 223 (Wang et al., 2018). This is also the case in our work where the Random Forest tech-  
 224 nique provides lower MAE and MAPE than the Neural Network. Furthermore, the Ran-  
 225 dom Forest training process was roughly  $\sim 20$  times computationally more efficient than  
 226 the training process of the Neural Network. As the XGBoost is even more advanced than  
 227 Random Forest technique, it was expected to outperform the Random Forest approach.  
 228 This assumption was confirmed and the best-performing technique in our work was the  
 229 XGBoost. The MAPE for green and red airglow lines were 16% and 32%, respectively.  
 230 The visualization of XGBoost performance on the testing subset is displayed in Figure  
 231 2. Considering the data measurement uncertainty level of 10–15% (Fishkova, 1983), the  
 232 machine learning model performs sufficiently well to qualitatively express the airglow vari-  
 233 ations. It is noted, the fact that the performance of almost all techniques is better for  
 234 the green airglow line than for the red airglow line might be explained by the following  
 235 consideration. The red atomic oxygen emission is strongly dependent on the electron den-  
 236 sity in the ionospheric F2 region. The green atomic oxygen emission is mainly depen-  
 237 dent on densities of neutral species (such as O, O<sub>2</sub> and N<sub>2</sub>) in the lower thermosphere.  
 238 Both regions are continuously affected by various unpredictable dynamical processes de-  
 239 termined by atmospheric waves and tidal motions. However, the amplitude of atmospheric  
 240 waves and magnitude of wind velocity is higher at the altitude of the red line luminous  
 241 layer. Therefore red line intensities have higher standard deviation than green line in-  
 242 tensities. This might be reflected also in higher MAPE for red line intensities.

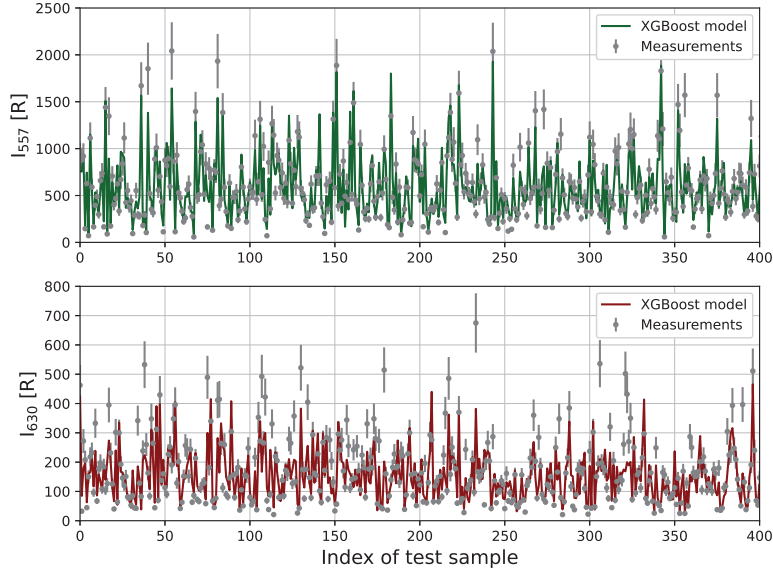


**Figure 2.** The performance of XGBoost model on the testing subset for green (top) and red (bottom) airglow lines intensities. The samples for the testing subset were selected randomly from all the available data. Only half of the testing subset is displayed to provide better visualization. The accuracy of the model against measurements is expressed in Table 2.

243 The results of the modeled intensities for green and red airglow lines over the whole  
 244 studied period 1964–1993 is in Figure 3. The modeled values were obtained using all avail-  
 245 able needed input features and by the prediction of the trained machine learning model  
 246 which is based on the XGBoost technique. Figure 3 represents the achievement of one  
 247 of this work’s goals as it contains averaged intensities of green and red airglow lines for  
 248 46,223 hours i.e. for 100% of all dark night hours within 1964–1993 period. Figure 3 serves  
 249 as the visualization of the green and red airglow lines intensities variations that are dis-  
 250 played for a continuous period over three solar cycles. To our knowledge, airglow vari-  
 251 ation visualization for a such long period and such time resolution has not been published  
 252 thus far.

253 To examine the credibility of the results generated by our machine learning model,  
 254 we have compared them with the results of the GLOW model (Hirsch & Solomon, 2019).  
 255 These results were obtained by the default setup of the GLOW model while we speci-  
 256 fied only the time, latitude and longitude. The calculated volume emission rates were  
 257 integrated over all altitudes to achieve values that might be compared with the measured

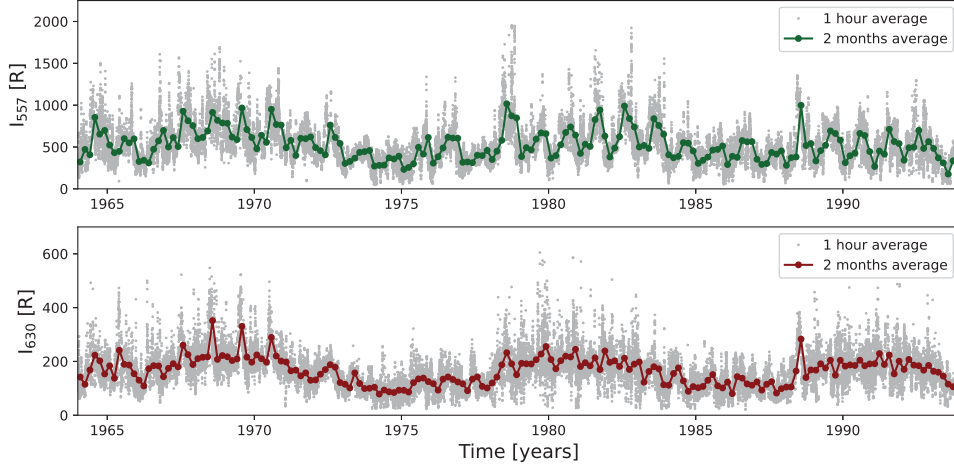


**Figure 3.** Visualization of airglow intensities modeled by the XGBoost technique for the location Abastumani (Georgia) over the years 1964–1993. The averages over 1 hour and 2 months for green (*top*) and red (*bottom*) airglow lines are displayed. Only dark night hours are considered.

258 airglow data. For the same testing dataset as was used for Table 2, the GLOW model  
 259 achieved as follows for the green line: MAE equals 280 R and MAPE equals 89%, for the  
 260 red line: MAE equals 109 R and MAPE equals 84%. These values are not as good as the  
 261 results of our machine learning model. This can be explained by the fact that the par-  
 262 ticular measured data might be influenced by phenomena that are not considered in the  
 263 default setup of the GLOW model. The performance of our machine learning model and  
 264 the GLOW model is presented in Figure 4 for the full period 1964–1993. This shows that  
 265 both models are qualitatively in good agreement. The correlation coefficients of simu-  
 266 lated intensities for the GLOW model and our machine learning model based on XG-  
 267 Boost averaged over 2 months and considering a linear least-squares regression are 0.48  
 268 and 0.54 for green and red line, respectively. It is an important result that the data-driven  
 269 model can provide valuable results even with a comparison of the physical model gen-  
 270 erally used. Even-more, as displayed in Figure 4, the data-driven model is less uniform  
 271 than the physical model and might be more consistent with the real variability expressed  
 272 by the measurements. However, it is important to note, the GLOW model is much more  
 273 general than the particular data-driven model and can be used for any location and time  
 274 because it does not require any measured airglow data for the input.

275 To examine the performance of our data-driven model for the completely unseen  
276 time period, we made an experiment where we split the main dataset for the subset for  
277 training and testing covering the years 1964–1979 (i.e. 50% of the previously used dataset)  
278 and for the subset for validation covering the years 1979–1993. The new model was trained  
279 and tested by using the training and testing subsets only. Its performance was then in-  
280 vestigated by the validation subset. The MAE and MAPE for the green airglow line were  
281 298 R and 99%, respectively. The MAE and MAPE for the red airglow line were 90 R  
282 and 95%, respectively. The mean errors are significantly higher than values in Table 2  
283 but this was expected because we used only data from a 15-year period for the training  
284 and testing process. The metrics for the GLOW model by using the same validation dataset  
285 were very similar. The MAE and MAPE for the green airglow line were 290 R and 105%,  
286 respectively. The MAE and MAPE for the red airglow line were 119 R and 100%, respec-  
287 tively. This demonstrates that for a completely unseen time period our data-driven ap-  
288 proach is still able to produce comparable results to the GLOW model. The correlation  
289 coefficients are now equal to 0.46 and 0.8 for the green and red line, respectively. It is  
290 interesting that the correlation coefficient for the red line is now significantly higher. This  
291 means that when we used less data for training of our model its results for the red line  
292 have a greater similarity to the results of the GLOW model. It is rather a surprising re-  
293 sult, because it might be expected that for the smaller training dataset the data-driven  
294 model would depart more from the GLOW model. The obvious explanation is that the  
295 GLOW model as well as our model trained on only a 15-year period do not consider all  
296 the phenomena that influence atomic oxygen airglow emissions. There is also a possi-  
297 ble explanation that airglow measurements acquired during the solar cycle number 22  
298 (1986–1996) were somehow different from the data acquired during the previous two so-  
299 lar cycles. This can be caused by the unknown contamination of the data or by occur-  
300 rence of some unique processes that produced unexpected airglow intensities. We will  
301 investigate this inconsistency in the future by comparison with airglow measurements  
302 from other locations for the similar time period.

303 Another examination of the credibility of our machine learning model is its abil-  
304 ity to express the airglow variations briefly presented in Section 1. As all inputs for the  
305 data-driven model are modulated directly or indirectly by the cycle of solar activity and  
306 the seasons, it is not a surprise that these variations should be present also in modeled  
307 airglow intensities. It is examined if the characteristics of these variations are compat-

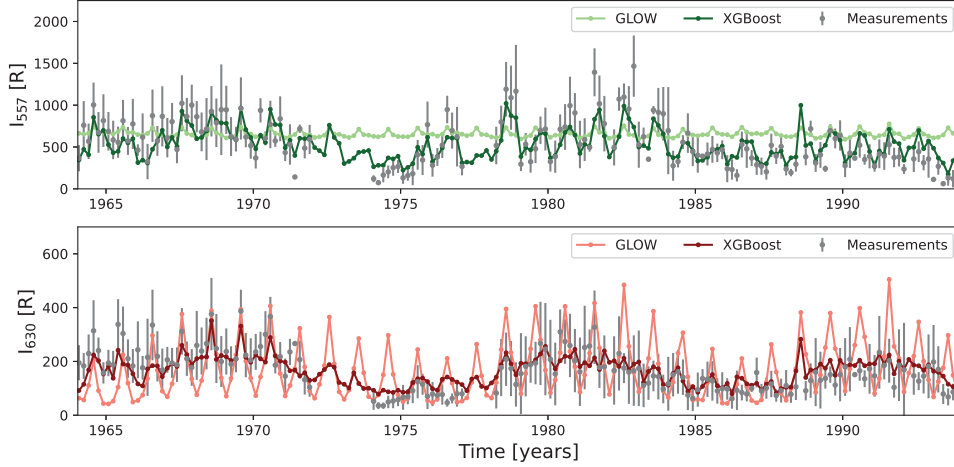


**Figure 4.** The time series of green (*top*) and red (*bottom*) airglow lines for the period 1964–1993. The 2-month averages of calculated intensities using the GLOW model and our data-driven model based on the XGBoost technique. The 2-month averages of measurements from Abastumani (Georgia) (see Figure 1) are displayed together with their standard deviations.

308     ible with the results of other authors. The airglow modulation by an 11-year solar cy-  
 309     cle is visible in Figure 3 at a glance. The green and red airglow lines intensities are max-  
 310     imal for the periods around the maxima of solar activity in the years 1969, 1980, and  
 311     1991, which is consistent with results presented in studies (e.g. Deutsch & Hernandez,  
 312     2003; Reid et al., 2014). The annual variation can be also recognized in Figure 3. Ac-  
 313     cording to previous studies (Shepherd et al., 2006) this variation of green line intensi-  
 314     ties should have its minimum in spring and maximum in autumn for the considered lo-  
 315     cation in the middle latitudes of the northern hemisphere. The results of our data-driven  
 316     model presented in Figure 5 (*top*) are consistent with these studies. The assumption for  
 317     the red airglow line for the considered location is that the maximum average intensity  
 318     should be in summer and the minimum near equinoxes (Khomich et al., 2008). The re-  
 319     sults presented in Figure 5 (*bottom*) are also consistent with this assumption. We note,  
 320     there are many more airglow variations present in Figures 3 and 5. They might be rec-  
 321     ognized by further investigation of the developed data-driven model results. These anal-  
 322     yses and comparison with various measurements, as done by other authors (e.g. Deutsch  
 323     & Hernandez, 2003; Gudadze et al., 2008), are objectives for future publication.

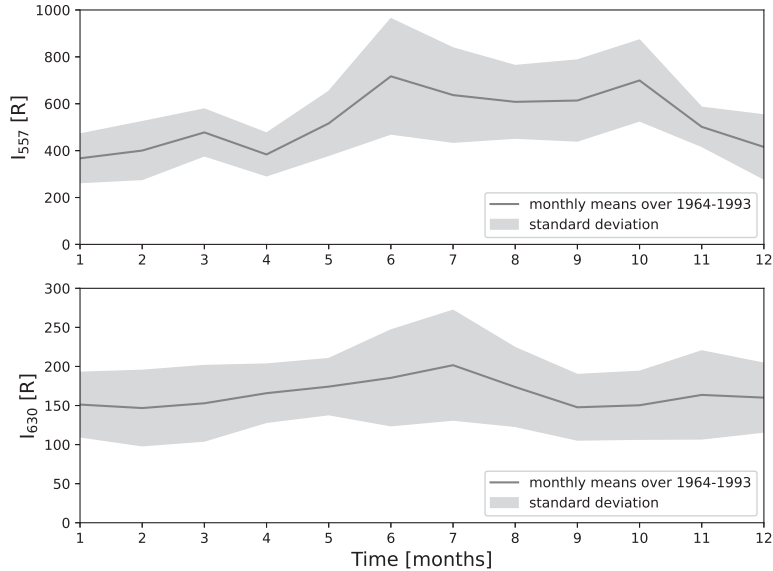


**Figure 5.** The average intensities calculated by a data-driven model based on the XGBoost technique for Abastumani (Georgia). The intensities were averaged over a particular month and for the years 1964–1993. The standard deviations from the mean values over the years are also displayed.

#### 324 4 Conclusions

325 Space data are of irreplaceable value as they provide information about phenom-  
 326 ena that can not be repeated. However, the occurrence of missing measurements and gaps  
 327 in the time series is very common. This is especially true for the ground-based measure-  
 328 ments where the observations are limited by the weather conditions. We have used the  
 329 most recent machine learning techniques to solve the regression problem and to model  
 330 the missing intensities of green and red airglow lines for the location Abastumani (Geor-  
 331 gia) over the time period 1964–1993. For this purpose, a data-driven approach was used.  
 332 The photometric airglow measurements were used as the labels (target outputs) and space  
 333 weather indices, thermosphere-ionosphere parameters, and Sun-Earth distances were used  
 334 as the features (inputs). The techniques of Linear Regression, Neural Network, Random  
 335 Forest, and XGBoost were employed and their performance was compared against the  
 336 testing dataset. The model based on the XGBoost technique outperformed the others  
 337 and provided mean absolute percentage error (MAPE) of 16% and 32% for the green and  
 338 red airglow lines, respectively. This performance is sufficient to qualitatively express the



339 overall airglow variation, and enables the modeled data to represent the missing mea-  
340 surements with a reasonable level of uncertainty. The obtained data visualize the vari-  
341 ations in the intensities of the green and red airglow lines over the period of three so-  
342 lar cycles. The results from the data-driven model are consistent with the GLOW model  
343 (Solomon, 2017) and depict the main variations related to solar activity and the seasons.

344 The modeled airglow data might contribute to understanding the processes in the  
345 interface region between the space environment and Earth’s atmosphere. Even more, the  
346 absolute values of airglow intensities and the range of their variation are crucial for fu-  
347 ture missions like EUSO-SPB2 (Wiencke, 2019) and POEMMA (NASA Probe Study re-  
348 port, 2020; Anchoordoqui et al., 2020). These missions are designed to observe extensive  
349 air showers induced by ultra-high energy cosmic rays and to observe Cherenkov light in-  
350 duced by cosmic neutrinos. Indeed, airglow emissions set the energy threshold of the events  
351 that could be recognized in the Earth’s night atmosphere by observation from orbit (JEM-  
352 EUSO collaboration, 2019; Krizmanic, 2021). For this purpose we plan to extend the vi-  
353 sualization of the airglow intensities for the years 1994–2020 as the input features should  
354 be available. We would like to also focus on the short time periods when the airglow in-  
355 tensities were significantly high and to investigate the possible explanations of these spe-  
356 cific events.

### 357 **Acknowledgments**

358 These airglow studies are supported by the government of Slovakia through the ESA con-  
359 tracts No. 4000125330/18/NL/SC and No. 4000125987/18/NL/SC under the PECS (Plan  
360 for European Cooperating States). ESA Disclaimer: The view expressed herein can in  
361 no way be taken to reflect the official opinion of the European Space Agency. The stud-  
362 ies of Sun-Earth connection are supported by the VEGA grant agency project 2/0155/18.  
363 The work is also supported by the Slovak Academy of Sciences MVTs JEM-EUSO grant.  
364 The studies related to machine learning techniques are supported by GlobalLogic Slo-  
365 vakia s.r.o. G. Didebulidze is supported by the Georgian Shota Rustaveli National Sci-  
366 ence Foundation Grant no. FR17–357. Data Availability Statement: The airglow data  
367 were provided by G. Didebulidze and are publicly available through the NDMC database  
368 (<https://ndmc.dlr.de>). The data of space weather, thermosphere, and ionosphere param-  
369 eters are publicly available through the NASA data centers (<https://omniweb.gsfc.nasa.gov>,

370 <https://ccmc.gsfc.nasa.gov>). The presented results can be reproduced by the Jupyter note-  
 371 book publicly available at <https://doi.org/10.5281/zenodo.4306913>.

## 372 References

- 373 Abadi, M., Agarwal, A., Barham, P., Brevdo, E., Chen, Z., Citro, C., . . . Zheng, X.  
 374 (2015). *TensorFlow: Large-scale machine learning on heterogeneous systems*.  
 375 (Software available from tensorflow.org)
- 376 Anchordoqui, L. A., Bergman, D. R., Bertaina, M. E., Fenu, F., Krizmanic,  
 377 J. F., Liberatore, A., . . . Wiencke, L. (2020, January). Performance  
 378 and science reach of the Probe of Extreme Multimessenger Astrophysics  
 379 for ultrahigh-energy particles. *Physical Review D*, *101*(2), 023012. doi:  
 380 10.1103/PhysRevD.101.023012
- 381 Bag, T., Singh, V., & Krishna, M. S. (2017). Study of atomic oxygen greenline day-  
 382 glow emission in thermosphere during geomagnetic storm conditions. *Advances*  
 383 *in Space Research*, *59*(1), 302 - 310. doi: <https://doi.org/10.1016/j.asr.2016.08>  
 384 .037
- 385 Ball, N. M., & Brunner, R. J. (2010, January). Data Mining and Machine Learning  
 386 in Astronomy. *International Journal of Modern Physics D*, *19*(7), 1049-1106.  
 387 doi: 10.1142/S0218271810017160
- 388 Bilitza, D., Altadill, D., Truhlik, V., Shubin, V., Galkin, I., Reinisch, B., & Huang,  
 389 X. (2017). International reference ionosphere 2016: From ionospheric cli-  
 390 mate to real-time weather predictions. *Space Weather*, *15*(2), 418-429. doi:  
 391 <https://doi.org/10.1002/2016SW001593>
- 392 Breiman, L. (2001). Random forests. *Machine Learning*, *45*(1), 5-32. doi: 10.1023/  
 393 A:1010933404324
- 394 Camporeale, E., Wing, S., & Johnson, J. (2018). *Machine learning techniques for*  
 395 *space weather*. Elsevier. doi: <https://doi.org/10.1016/C2016-0-01976-9>
- 396 Chen, T., & Guestrin, C. (2016). XGBoost: A scalable tree boosting system. In  
 397 *Proceedings of the 22nd acm sigkdd international conference on knowledge*  
 398 *discovery and data mining* (pp. 785–794). New York, NY, USA: ACM. doi:  
 399 10.1145/2939672.2939785
- 400 Chollet, F. e. a. (2015). *Keras*. <https://keras.io>.
- 401 Cybenko, G. (1989, December 1). Approximation by superpositions of a sigmoidal

- 402 function. *Mathematics of Control, Signals, and Systems (MCSS)*, 2(4), 303–  
403 314. doi: 10.1007/BF02551274
- 404 Deutsch, K. A., & Hernandez, G. (2003, December). Long-term behavior of the OI  
405 558 nm emission in the night sky and its aeronomical implications. *Journal of*  
406 *Geophysical Research (Space Physics)*, 108, 1430. doi: 10.1029/2002JA009611
- 407 Didebulidze, G. G., Lomidze, L. N., Gudadze, N. B., Pataraya, A. D., & Todua, M.  
408 (2011). Long-term changes in the nightly behaviour of the oxygen red 630.0  
409 nm line nightglow intensity and trends in the thermospheric meridional wind  
410 velocity. *International Journal of Remote Sensing*, 32(11), 3093-3114. doi:  
411 10.1080/01431161.2010.541523
- 412 Eastes, R. W., McClintock, W. E., Burns, A. G., Anderson, D. N., Andersson, L.,  
413 Codrescu, M., ... Oberheide, J. (2017, October). The Global-Scale Observa-  
414 tions of the Limb and Disk (GOLD) Mission. *Space Sci. Rev.*, 212, 383-408.  
415 doi: 10.1007/s11214-017-0392-2
- 416 Eastes, R. W., Solomon, S. C., Daniell, R. E., Anderson, D. N., Burns, A. G., Eng-  
417 land, S. L., ... McClintock, W. E. (2019). Global-scale observations of the  
418 equatorial ionization anomaly. *Geophysical Research Letters*, 46(16), 9318-  
419 9326. doi: 10.1029/2019GL084199
- 420 Fernández-Delgado, M., Cernadas, E., Barro, S., & Amorim, D. (2014). Do we need  
421 hundreds of classifiers to solve real world classification problems? *Journal of*  
422 *Machine Learning Research*(15), 3133-3181.
- 423 Fishkova, L. M. (1983). *The night airglow of the earth mid-latitude upper atmo-*  
424 *sphere*.
- 425 Gan, Q., Eastes, R. W., Burns, A. G., Wang, W., Qian, L., Solomon, S. C., ... Mc-  
426 Clintock, W. E. (2020). First synoptic observations of geomagnetic storm  
427 effects on the global-scale oi 135.6-nm dayglow in the thermosphere by the  
428 gold mission. *Geophysical Research Letters*, 47(3), e2019GL085400. doi:  
429 10.1029/2019GL085400
- 430 George, D., & Huerta, E. (2018). Deep learning for real-time gravitational wave  
431 detection and parameter estimation: Results with advanced ligo data. *Physics*  
432 *Letters B*, 778, 64 - 70. doi: <https://doi.org/10.1016/j.physletb.2017.12.053>
- 433 Gudadze, N. B., Didebulidze, G. G., Javakhishvili, G. S., Shepherd, M. G., & Var-  
434 dosanidze, M. V. (2007, February). Long-term variations of the oxygen red 630

- 435 nm line nightglow intensity. *Canadian Journal of Physics*, *85*(2), 189-198. doi:  
436 10.1139/P07-032
- 437 Gudadze, N. B., Didebulidze, G. G., Lomidze, L. N., Javakhishvili, G. S., Marsag-  
438 ishvili, M. A., & Todua, M. (2008). Different long-term trends of the  
439 oxygen red 630.0 nm line nightglow intensity as the result of lowering  
440 the ionosphere f2 layer. *Annales Geophysicae*, *26*(8), 2069-2080. doi:  
441 10.5194/angeo-26-2069-2008
- 442 Hannawald, P., Schmidt, C., Sedlak, R., Wüst, S., & Bittner, M. (2019). Seasonal  
443 and intra-diurnal variability of small-scale gravity waves in oh airglow at two  
444 alpine stations. *Atmospheric Measurement Techniques*, *12*(1), 457-469. doi:  
445 10.5194/amt-12-457-2019
- 446 Hirsch, M., & Solomon, S. (2019, September). *space-physics/ncar-glow*. Zenodo. doi:  
447 10.5281/zenodo.3463662
- 448 Immel, T. J., England, S. L., Mende, S. B., Heelis, R. A., Englert, C. R., Edel-  
449 stein, J., . . . Sirk, M. M. (2018, February). The Ionospheric Connection  
450 Explorer Mission: Mission Goals and Design. *Space Sci. Rev.*, *214*, 13. doi:  
451 10.1007/s11214-017-0449-2
- 452 Isobe, T., Feigelson, E. D., Akritas, M. G., & Babu, G. J. (1990, November). Linear  
453 Regression in Astronomy. I. *Astrophys. J.*, *364*, 104. doi: 10.1086/169390
- 454 JEM-EUSO collaboration. (2019, September). Ultra-violet imaging of the  
455 night-time earth by EUSO-Balloon towards space-based ultra-high en-  
456 ergy cosmic ray observations. *Astroparticle Physics*, *111*, 54-71. doi:  
457 10.1016/j.astropartphys.2018.10.008
- 458 Khomich, V. Y., Semenov, A. I., & Shefov, N. N. (2008). *Airglow as an Indicator of*  
459 *Upper Atmospheric Structure and Dynamics*. Springer-Verlag.
- 460 King, J. H., & Papitashvili, N. E. (2005). Solar wind spatial scales in and compar-  
461 isons of hourly wind and ace plasma and magnetic field data. *Journal of Geo-*  
462 *physical Research: Space Physics*, *110*(A2). doi: 10.1029/2004JA010649
- 463 Krizmanic, J. F. (2021). Space-based extensive air shower optical cherenkov  
464 and fluorescence measurements using sipm detectors in context of poemma.  
465 *Nuclear Instruments and Methods in Physics Research Section A: Accelera-*  
466 *tors, Spectrometers, Detectors and Associated Equipment*, *985*, 164614. doi:  
467 <https://doi.org/10.1016/j.nima.2020.164614>

- 468 Leonovich, L. A., Mikhalev, A. V., & Leonovich, V. A. (2011, Aug 17). The 557.7  
469 and 630-nm atomic oxygen midlatitude airglow variations associated with  
470 geomagnetic activity. *Atmospheric and Oceanic Optics*, *24*(4), 396. doi:  
471 10.1134/S1024856011040105
- 472 Liu, G., & Shepherd, G. G. (2008). An investigation of the solar cycle impact on the  
473 lower thermosphere o(1s) nightglow emission as observed by windii/uars. *Ad-  
474 vances in Space Research*, *42*(5), 933 - 938. doi: [https://doi.org/10.1016/j.asr.  
475 .2007.10.008](https://doi.org/10.1016/j.asr.2007.10.008)
- 476 Liu, G., Shepherd, G. G., & Roble, R. G. (2008). Seasonal variations of the night-  
477 time o(1s) and oh airglow emission rates at mid-to-high latitudes in the con-  
478 text of the large-scale circulation. *Journal of Geophysical Research: Space  
479 Physics*, *113*(A6). doi: 10.1029/2007JA012854
- 480 Mackovjak, Š., Bobík, P., Baláz, J., Strhářský, I., Putiš, M., & Gorodetzky,  
481 P. (2019, April). Airglow monitoring by one-pixel detector. *Nuclear  
482 Instruments and Methods in Physics Research A*, *922*, 150-156. doi:  
483 10.1016/j.nima.2018.12.073
- 484 Makela, J. J., Harding, B. J., Meriwether, J. W., Mesquita, R., Sanders, S., Ridley,  
485 A. J., ... Martinis, C. R. (2014). Storm time response of the midlatitude  
486 thermosphere: Observations from a network of fabry-perot interferometers.  
487 *Journal of Geophysical Research: Space Physics*, *119*(8), 6758-6773. doi:  
488 10.1002/2014JA019832
- 489 NASA Probe Study report. (2020). *POEMMA: Probe of Extreme Multi-Messenger  
490 Astrophysics*. [https://smd-prod.s3.amazonaws.com/science-pink/  
491 s3fs-public/atoms/files/1\\_POEMMA\\_Study\\_Rpt\\_0.pdf](https://smd-prod.s3.amazonaws.com/science-pink/s3fs-public/atoms/files/1_POEMMA_Study_Rpt_0.pdf).
- 492 NDMC. ((last access: November 30, 2020)). *The Network for the Detection of Meso-  
493 spheric Change (NDMC)*, available at. <https://ndmc.dlr.de>.
- 494 Paszke, A., Gross, S., Chintala, S., Chanan, G., Yang, E., DeVito, Z., ... Lerer, A.  
495 (2017). *Automatic differentiation in pytorch*.
- 496 Pedregosa, F., Varoquaux, G., Gramfort, A., Michel, V., Thirion, B., Grisel, O., ...  
497 Duchesnay, E. (2011). Scikit-learn: Machine learning in Python. *Journal of  
498 Machine Learning Research*, *12*, 2825–2830.
- 499 Pfaff, R. F. (2012, June). The Near-Earth Plasma Environment. *Space Sci. Rev.*,  
500 *168*, 23-112. doi: 10.1007/s11214-012-9872-6

- 501 Picone, J. M., Hedin, A. E., Drob, D. P., & Aikin, A. C. (2002). Nrlmsise-00 em-  
 502 pirical model of the atmosphere: Statistical comparisons and scientific issues.  
 503 *Journal of Geophysical Research: Space Physics*, *107*(A12), SIA 15-1-SIA  
 504 15-16. doi: 10.1029/2002JA009430
- 505 Qian, L., Burns, A. G., Emery, B. A., Foster, B., Lu, G., Maute, A., ... Wang,  
 506 W. (2014). The near tie-gcm. In *Modeling the ionosphere-thermosphere*  
 507 *system* (p. 73-83). American Geophysical Union (AGU). doi: 10.1002/  
 508 9781118704417.ch7
- 509 Rayleigh, L., & Jones, H. S. (1935, Aug). The Light of the Night-Sky: Analysis of  
 510 the Intensity Variations at Three Stations. *Proceedings of the Royal Society of*  
 511 *London Series A*, *151*(872), 22-55. doi: 10.1098/rspa.1935.0133
- 512 Reid, I. M., Spargo, A. J., & Woithe, J. M. (2014). Seasonal variations of the  
 513 nighttime O (1S) and OH (8-3) airglow intensity at Adelaide, Australia.  
 514 *Journal of Geophysical Research: Atmospheres*, *119*(11), 6991-7013. doi:  
 515 10.1002/2013JD020906
- 516 Roble, R. G., Ridley, E. C., Richmond, A. D., & Dickinson, R. E. (1988). A coupled  
 517 thermosphere/ionosphere general circulation model. *Geophysical Research Let-*  
 518 *ters*, *15*(12), 1325-1328. doi: 10.1029/GL015i012p01325
- 519 Shepherd, G., Thuillier, G., Gault, W., Solheim, B., Hersom, C., Alunni, J., ...  
 520 Wimperis, J. (1993, 06). Windii, the wind imaging interferometer on the upper  
 521 atmosphere research satellite. *J. Geophys. Res.*, *98*. doi: 10.1029/93JD00227
- 522 Shepherd, G. G., Cho, Y.-M., Liu, G., Shepherd, M. G., & Roble, R. G. (2006,  
 523 December). Airglow variability in the context of the global mesospheric circu-  
 524 lation. *Journal of Atmospheric and Solar-Terrestrial Physics*, *68*, 2000-2011.  
 525 doi: 10.1016/j.jastp.2006.06.006
- 526 Silverman, S. M. (1970, October). Night Airglow Phenomenology. *Space Sci. Rev.*,  
 527 *11*, 341-379. doi: 10.1007/BF00241526
- 528 Solomon, S. C. (2017). Global modeling of thermospheric airglow in the far ultravi-  
 529 olet. *Journal of Geophysical Research: Space Physics*, *122*(7), 7834-7848. doi:  
 530 10.1002/2017JA024314
- 531 Solomon, S. C., Hays, P. B., & Abreu, V. J. (1988). The auroral 6300 Å emission:  
 532 Observations and modeling. *Journal of Geophysical Research: Space Physics*,  
 533 *93*(A9), 9867-9882. doi: 10.1029/JA093iA09p09867

- 534 SPACE::LAB. (2020, December). *space-lab-sk/airglow\_data-driven\_model: First re-*  
 535 *lease*. Zenodo. Retrieved from <https://doi.org/10.5281/zenodo.4306913>  
 536 doi: 10.5281/zenodo.4306913
- 537 Tin Kam Ho. (1998). The random subspace method for constructing decision  
 538 forests. *IEEE Transactions on Pattern Analysis and Machine Intelligence*,  
 539 *20*(8), 832-844.
- 540 Van Rossum, G., & Drake, F. L. (2009). *Python 3 reference manual*. Scotts Valley,  
 541 CA: CreateSpace.
- 542 von Savigny, C. (2017, Oct 17). Airglow in the earth atmosphere: basic characteris-  
 543 tics and excitation mechanisms. *ChemTexts*, *3*(4), 14. doi: 10.1007/s40828-017  
 544 -0051-y
- 545 Wang, S., Aggarwal, C., & Liu, H. (2018, 10). Random-forest inspired neural net-  
 546 works. *ACM Transactions on Intelligent Systems and Technology*, *9*. doi: 10  
 547 .1145/3232230
- 548 Wiencke, L. (2019, July). The Extreme Universe Space Observatory on a Super-  
 549 Pressure Balloon II Mission. In *36th international cosmic ray conference*  
 550 (*icrc2019*) (Vol. 36, p. 466).
- 551 Wüst, S., Schmidt, C., Hannawald, P., Bittner, M., Mlynczak, M. G., & Rus-  
 552 sell III, J. M. (2019). Observations of oh airglow from ground, aircraft,  
 553 and satellite: investigation of wave-like structures before a minor strato-  
 554 spheric warming. *Atmospheric Chemistry and Physics*, *19*(9), 6401–6418.  
 555 doi: 10.5194/acp-19-6401-2019
- 556 Zucker, S., & Gyries, R. (2018, mar). Shallow transits—deep learning. i. feasibility  
 557 study of deep learning to detect periodic transits of exoplanets. *The Astronom-*  
 558 *ical Journal*, *155*(4), 147. doi: 10.3847/1538-3881/aaae05

figure1.eps.



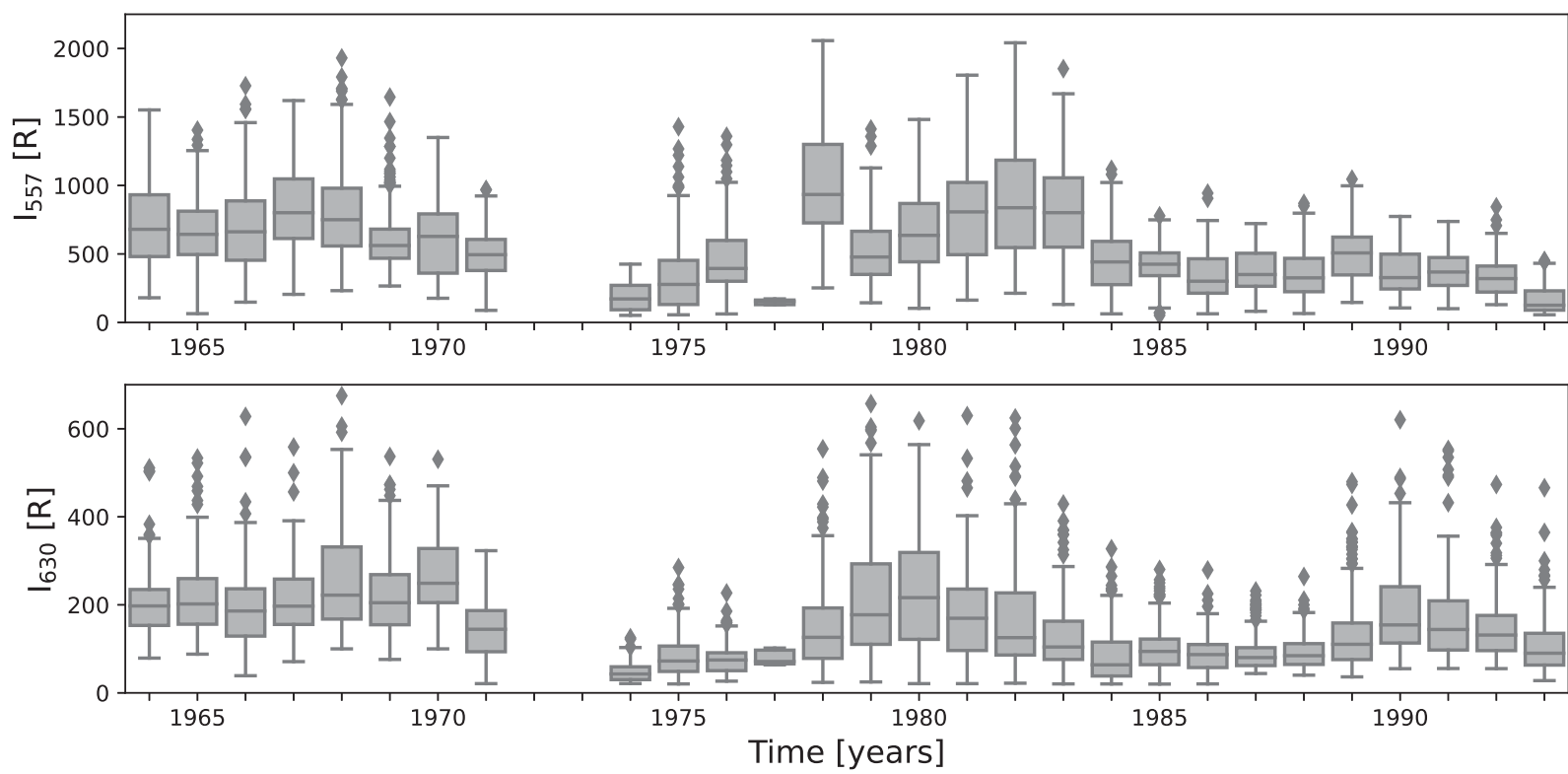


figure2.eps.

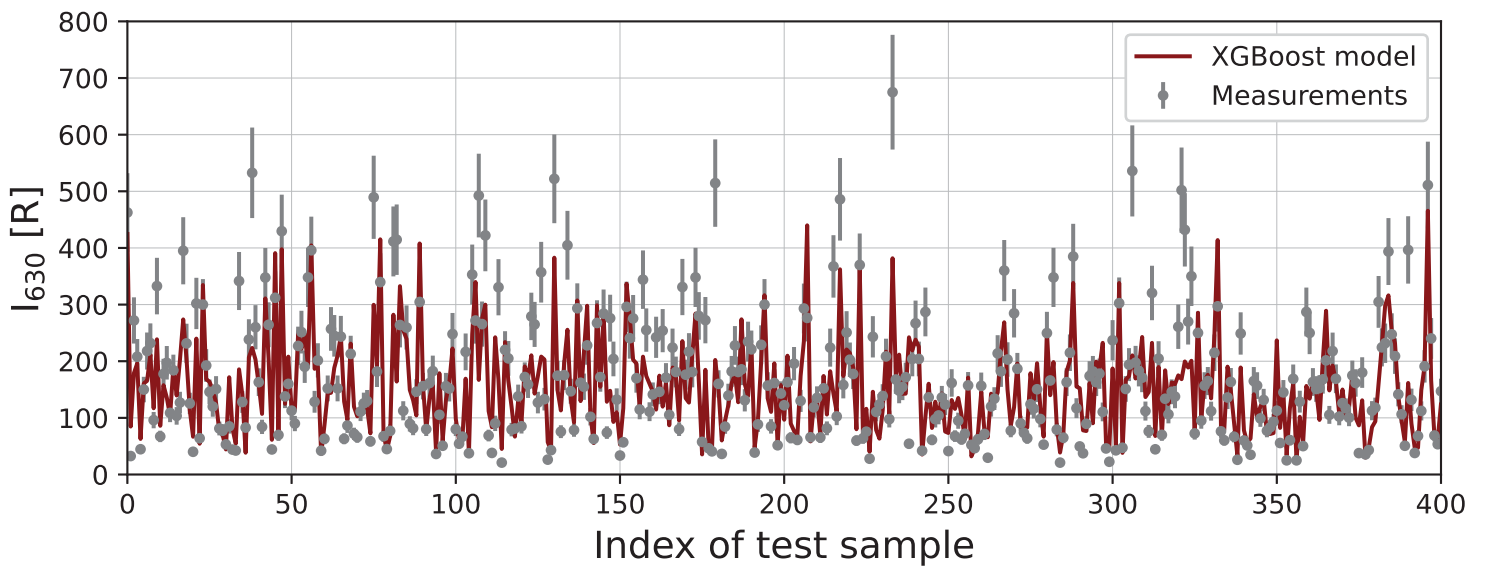
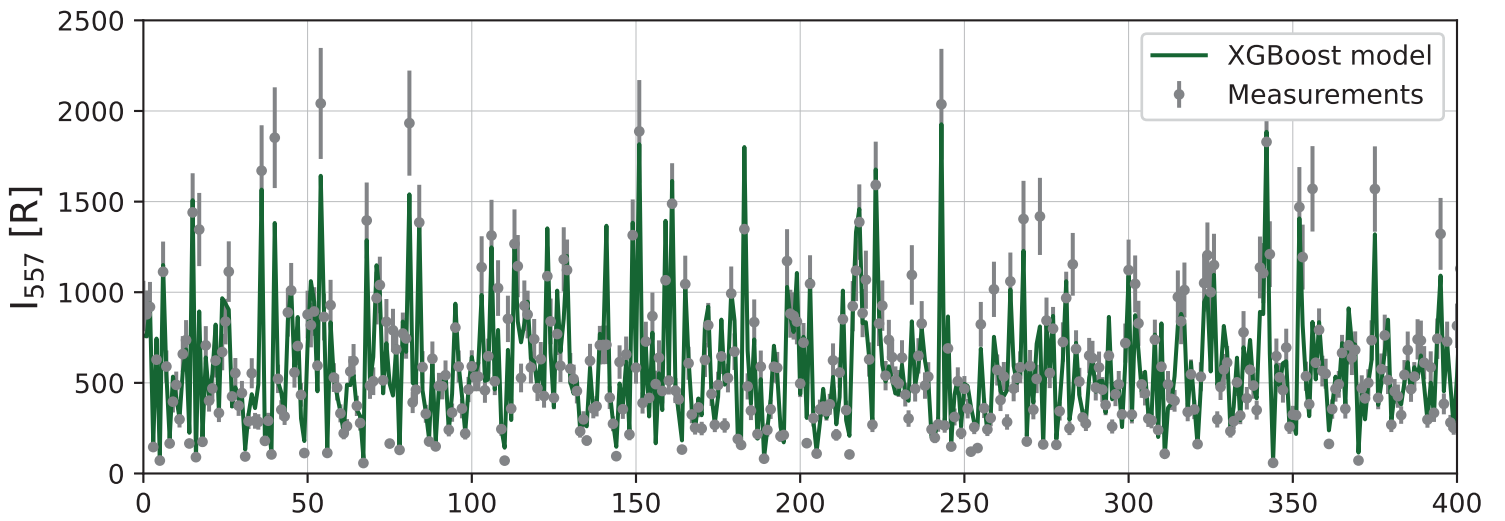


figure3.eps.

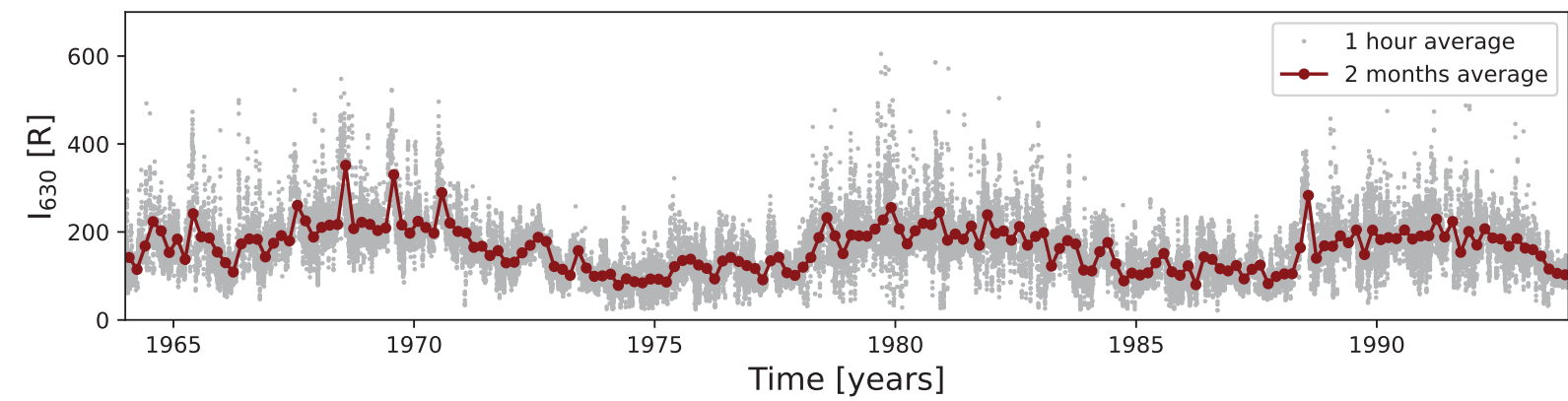
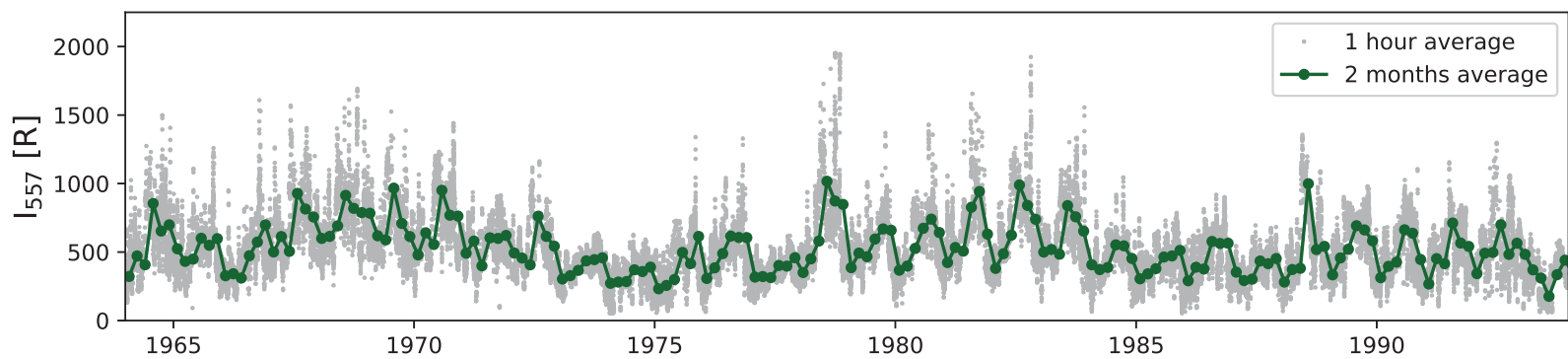


figure4.eps.

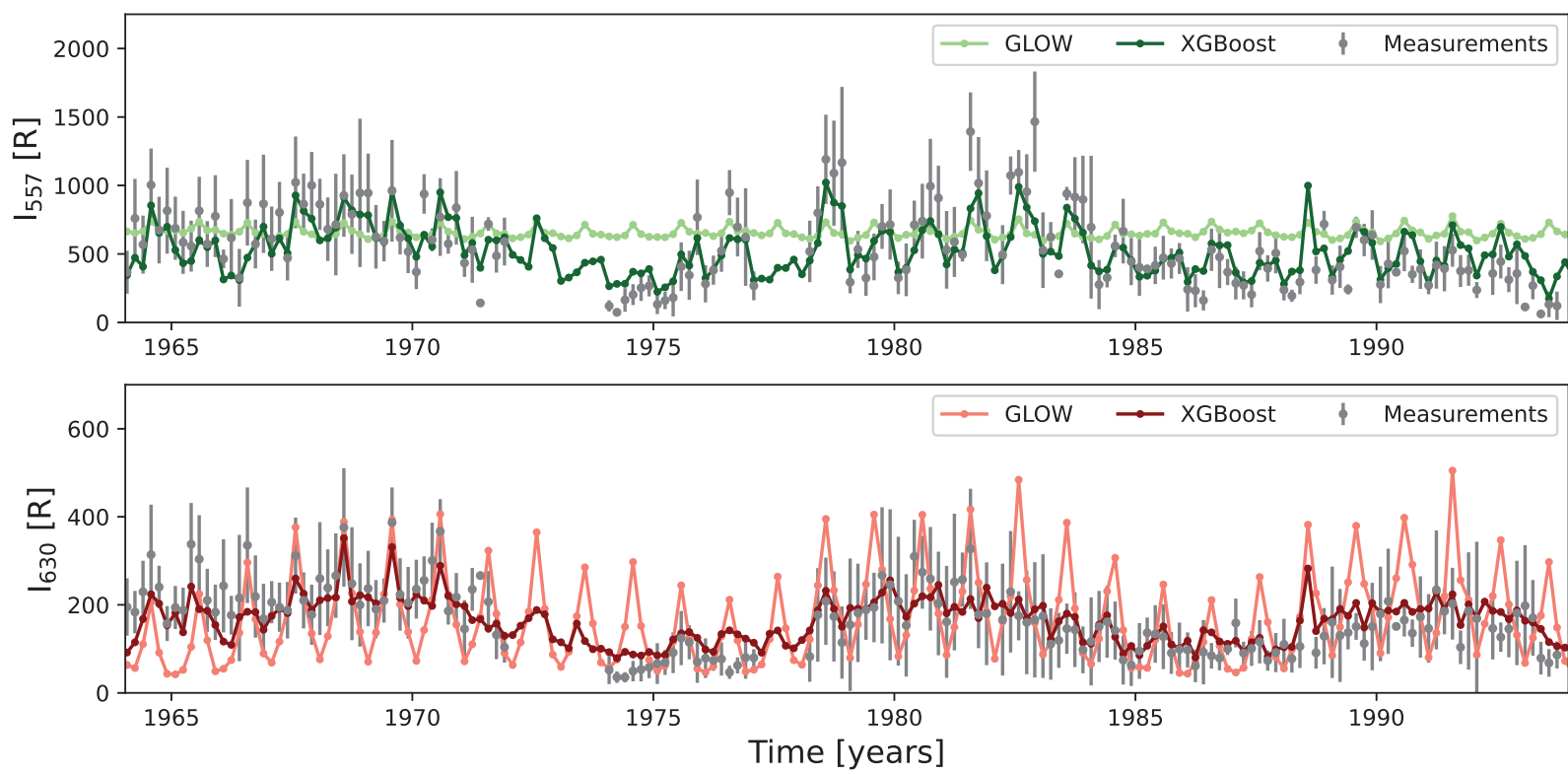


figure5.eps.



